Membrane and Water Treatment, *Vol. 17, No. 4 (2026) 277-291*
https://doi.org/10.12989/mwt.2026.17.4.277

Techno-Press

RSM optimization of stirred-cell membrane separation for O/W emulsions

Jingru Hu, Changjiang Zuo, Tonggang Hou*

Qingdao Technical College, Qingdao, Shandong, China

(Received February 3, 2026, Revised June 4, 2026, Accepted June 11, 2026)

Abstract. To mitigate membrane fouling effectively during the treatment of oil-in-water (O/W) emulsions, this study optimized a stirred-cell membrane filtration system using Response Surface Methodology (RSM) based on a Box-Behnken Design (BBD). The combined effects of the water-to-oil ratio, stirring rate, and transmembrane pressure (TMP) on permeate flux were systematically investigated. Analysis of Variance (ANOVA) results yielded a highly predictive quadratic model (R^2=0.9817). Critical interaction analyses revealed that increased stirring significantly reduces concentration polarization, whereas excessive TMP at low water-to-oil ratios induces pore blocking via oil droplet deformation. Numerical optimization identified the ideal operating conditions as a water-to-oil ratio of 8.5, a stirring rate of 213 rpm, and a TMP of 0.059 MPa. Validation experiments under these conditions achieved a permeate flux of 4.37 $L \cdot m^{-2} \cdot h^{-1}$ with an effluent oil content of <50 ppm. These findings provide essential hydrodynamic strategies for enhancing separation efficiency and controlling fouling in industrial applications.

Keywords: oil-water separation; process optimization; response surface methodology (RSM); stirred-cell membrane

1. Introduction

Oil-water separation is a critical unit operation in modern industrial production and environmental protection. Its efficiency directly impacts resource recovery, product quality, production costs, and pollution control [1]. Oil-water mixtures are prevalent in industries such as petrochemicals, food processing, pharmaceuticals, metalworking, and wastewater treatment. Specifically, processes such as the purification of fine chemical products involving multiple water-washing steps, or degumming, deacidification, and decolorization in vegetable oil refining, require the rapid and thorough separation of large volumes of oil-water mixtures [2]. A compelling example is the production of thionocarbamate, widely regarded as the “King of Reagents” in the global non-ferrous metal flotation industry [3, 4]. Its synthesis, typically via the sodium chloroacetate-sodium hydrosulfide route, necessitates multiple water-washing and separation cycles. The efficiency and quality of this separation step are pivotal to the purity of the final product, the operational efficiency of the production line, and the effective recovery of high-value materials. Consequently, developing novel oil-water separation technologies that balance efficiency, precision, and operational simplicity is of significant industrial value.

*Corresponding author, Professor, E-mail: houtg@qtc.edu.cn

ISSN: 2005-8624 (Print), 2092-7037 (Online)

Currently, the separation of thionocarbamate oil-water mixtures primarily relies on the traditional gravity settling stratification method. This method utilizes the density difference between oil and water to achieve natural separation of the two phases under static conditions [5]. Despite its theoretical simplicity, gravity settling faces insurmountable challenges in practical applications. Firstly, it is a time-consuming process, often requiring hours or days to achieve macroscopic stratification, thereby creating a bottleneck in production workflows. Furthermore, even in surfactant-free systems, mixing and transport can generate fine dispersed droplets [6]. These fine droplets coalesce slowly, often forming a stable, turbid intermediate layer known as the "rag layer" [7]. This emulsified layer occupies effective equipment volume and represents a significant loss of valuable product, reducing overall recovery rates. Additionally, the ambiguous interface makes accurate separation difficult, often leading to the entrainment of the dispersed phase into the clarified phase, necessitating subsequent purification steps. While alternatives like centrifugation and coalescers exist, they are often associated with high capital costs, energy consumption, or sensitivity to droplet size distribution.

To overcome these inherent limitations, membrane separation technology, characterized by high efficiency, low energy consumption, and environmental friendliness, has emerged as a promising alternative [8-10] for oil-water separation [11]. Utilizing a semi-permeable membrane, this technology achieves precise physical separation driven by a pressure gradient [12]. In the stirred-cell filtration system employed in this study, separation performance—particularly permeate flux—is influenced by coupled factors. Feed properties, such as the water-to-oil ratio (X_1), determine system viscosity and droplet collision probability [13]. Hydrodynamic conditions, specifically the stirring rate (X_2), dictate the shear environment at the membrane surface, playing a decisive role in mitigating concentration polarization and fouling [14]. Meanwhile, the transmembrane pressure (TMP, X_3) serves as the driving force for mass transfer but may also exacerbate cake layer compaction. Complex, non-linear relationships exist among these variables [15]. Traditional "One-Factor-At-a-Time" (OFAT) approaches fail to capture these critical interactions [16-18], highlighting the need for multivariate statistical optimization [19].

Therefore, this study employs Response Surface Methodology (RSM) to model, analyze, and optimize the stirred-cell membrane separation process[20]. To address these challenges, the primary objective of this study is to evaluate how permeate flux is influenced by key operational parameters, specifically the water-to-oil ratio (X_1), stirring rate (X_2), and transmembrane pressure (TMP, X_3). This is achieved by utilizing a Box-Behnken Design (BBD) to determine the significance of variable interactions and to develop a validated quadratic polynomial model for flux prediction. In addition, this research elucidates the underlying coupling mechanisms between hydrodynamics and feed composition through 3D response surface analysis. By integrating these methodological approaches, the study ultimately identifies and experimentally validates the optimal process conditions necessary for maximizing separation efficiency.

2. Methods and materials

2.1 Materials

The oil phase used in this study was high-purity thionocarbamate (Analytical Reagent, >99%), purchased from Qingdao LNT Chemical Co., LTD. The aqueous phase was laboratory-prepared deionized water. The original solution is a thermodynamically unstable microemulsion, which is

extremely difficult to separate by conventional gravity sedimentation. The membrane selected was a Labshark hydrophilic membrane made of polytetrafluoroethylene (PTFE), with a nominal pore size of 0.22 μm and an effective membrane area of 12.56 cm^2. The reagent used for membrane cleaning was anhydrous ethanol (AR, Analytical Reagent).

2.2 Experimental apparatus

The experiments were conducted in a 250-mL stirred-cell ultrafiltration unit (schematic diagram omitted). The system primarily consists of the following components:

Filtration Unit: A cell body equipped with a sintered glass support, where the flat-sheet membrane was placed at the bottom.

Agitation System: An FW2208F-5LD overhead stirrer employed to provide a precisely controlled shear rate (X_2).

Pressure Control System: An SHZ-95A circulating water vacuum pump coupled with a precision vacuum regulator to adjust the transmembrane pressure (TMP, X_3). Prior to each run, the feed emulsion was prepared according to the specified water-to-oil ratio (X_1) and loaded into the cell. To strictly simulate the actual industrial water-washing conditions of thionocarbamate, the feed emulsion was prepared using mild mechanical agitation rather than extreme high-shear homogenization. Specifically, the oil and aqueous phases were combined according to the specified water-to-oil ratio (X_1) and mixed using a conventional magnetic stirrer at a low speed of 100 rpm for 10 minutes prior to filtration. As confirmed by subsequent analysis (detailed in Section 3.5), this low-shear preparation standardizes a metastable emulsion with an average initial droplet size of 5-10 μm. Because these initial droplets are significantly larger than the membrane's nominal pore size (0.22 μm), the primary initial fouling mechanism is governed by reversible cake layer deposition [21]. This controlled preparation is a crucial prerequisite, as it isolates the initial droplet size effect, allowing us to systematically investigate how the varied filtration stirring rate (X_2) in the stirred-cell influences cake layer scouring and shear-induced droplet deformation. Permeate was collected in a vacuum flask, and all experiments were performed at 25°C.

New hydrophilic membrane discs were soaked in deionized water for 5 minutes prior to use. The initial pure water flux was standardized by measuring the time required to filter 100 mL of deionized water at 0.01 MPa.

2.3 Experimental design and RSM analysis (Design-Expert)

Based on the preliminary single-factor experimental results (detailed in Section 3.1), the effective ranges for each variable were determined. A Box-Behnken Design (BBD) involving three factors at three levels was employed (Table 1) [22]. The independent variables and their corresponding coded levels (−1, 0, +1) were established based on the findings from the single-factor experiments in Section 3.1.

According to the BBD model, a total of 17 experiments were required, including 12 factorial points and 5 replicates at the center point. The center point replicates were used to evaluate the pure error of the experiment. The order of all experiments was randomized.

Experimental data were analyzed using Design-Expert® software. Through multiple regression fitting, a quadratic polynomial model describing the relationship between the response value (Y) and the independent variables (X_1, X_2, X_3) was obtained, as shown in Eq. (1):

$$Y = \beta_0 + \sum_{i=1}^{k} \beta_i X_i + \sum_{i=1}^{k} \beta_{ii} X_i^2 + \sum_{i<j} \beta_{ij} X_i X_j + \epsilon \quad (1)$$

where Y is the predicted response value (Permeate flux), and β_0,β_i, β_{ii}, β_{ij} are the regression coefficients for the intercept, linear, quadratic, and interaction terms, respectively. The significance of the model was tested using Analysis of Variance (ANOVA).

2.4 Separation experiments and data collection

The permeation flux (J, L m^{-2} h^{-1}) was calculated using Eq. (2) [23]:

$$J=V/(A\cdot t) \quad (2)$$

where V is the permeate volume, A is the effective membrane area, and t is the time. To minimize transient fluctuations, the average flux measured at 1 minute of operation was used as the response variable. The oil content in the aqueous phase was determined via Infrared Spectrophotometry (HJ 637-2018).

3. Results and discussion

3.1 Single-factor experiments and comparative analysis of variable sensitivities

Prior to the BBD design, single-factor experiments were systematically conducted to screen the effective ranges of the three independent variables and reveal the dominant fouling mechanism associated with each variable. The results are summarized in Fig. 1(a-c).

The water-to-oil ratio (X_1, Fig. 1a) controls bulk emulsion viscosity and the volumetric oil load reaching the membrane surface. As the oil fraction increased (X_1 decreased from 10 to 6), the permeate flux declined by approximately 11.24%, primarily because of the rapid build-up of a denser cake layer and intensified concentration polarization. Above $X_1 = 10$, the flux gain became marginal, indicating that the resistance had transitioned from a cake-controlled to a membrane-controlled regime. Therefore, $X_1 \in [8, 10]$ was selected.

The stirring rate (X_2, Fig. 1b) governs the wall shear rate and thus directly modulates the cake-layer thickness. In contrast to X_1, X_2 exhibits a non-monotonic response: flux first increased steeply from 0 to 190 rpm because shear stress effectively scoured loosely deposited oil droplets and suppressed concentration polarization, but it plateaued and even slightly declined beyond ~250 rpm. This inflection reflects a mechanistic transition. Under moderate shear, the average droplet size (5-10 μm, Section 3.5) is much larger than the membrane pore size (0.22 μm), so cake filtration is the dominant and reversible fouling mode. Once the wall shear stress exceeds the critical capillary number of the oil droplets ($Ca_c \approx$ 0.1-0.5 for low-viscosity ratios) [24-26], droplets fragment to sub-micrometre sizes and begin to penetrate the pores, switching the dominant mechanism to standard pore blocking, which is largely irreversible [27]. Hence $X_2 \in [0, 380]$ rpm was used to capture both regimes.

The transmembrane pressure (X_3, Fig. 1c) drives convective transport but also compacts the cake layer. In the low-pressure regime (≤0.06 MPa) the flux scales linearly with TMP, in agreement with Darcy's law for a constant-resistance medium. Above ~0.06 MPa, the flux

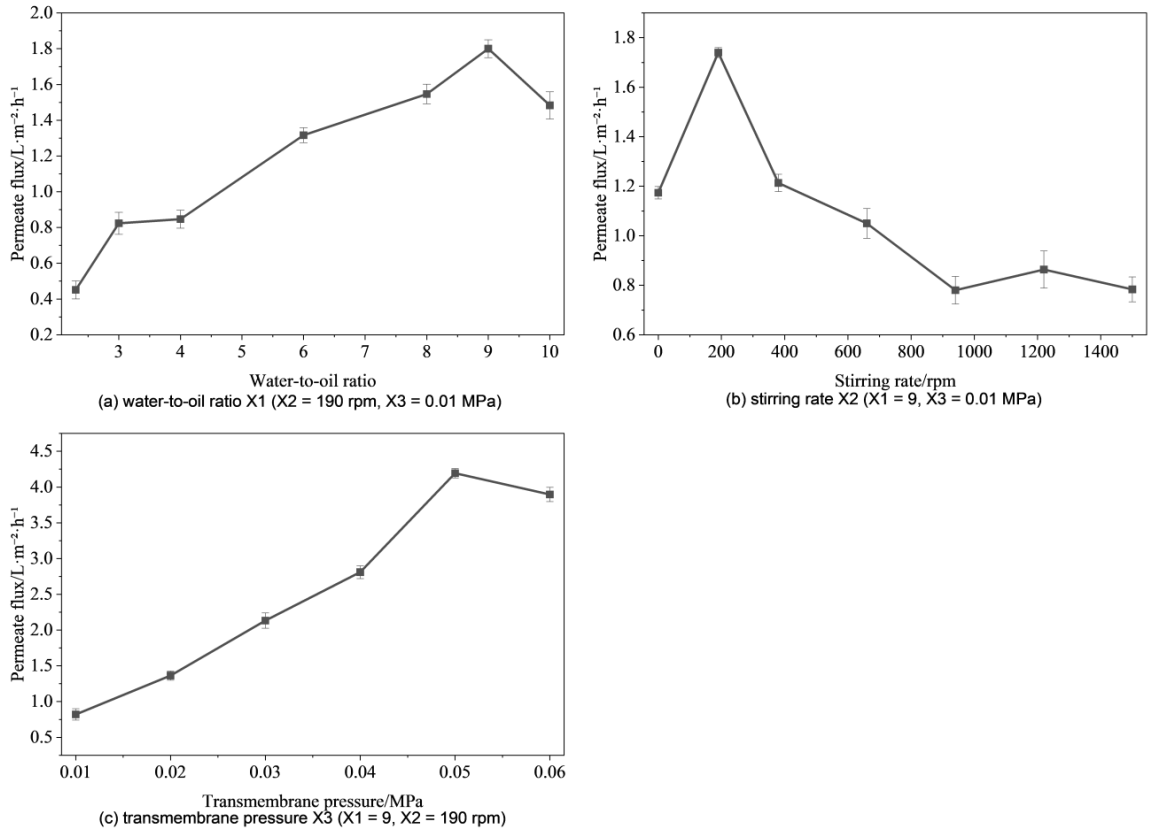

Figure 1. Single-factor effects on permeate flux: (a) water-to-oil ratio X_1 (X_2 = 190 rpm, X_3 = 0.01 MPa); (b) stirring rate X_2 (X_1 = 9, X_3 = 0.01 MPa); (c) transmembrane pressure X_3 (X_1 = 9, X_2 = 190 rpm). All experiments were performed at 25 °C with a 0.22 μm hydrophilic PTFE membrane

deviates downward and eventually plateaus, reflecting the well-known transition from pressure-controlled to mass-transfer-controlled filtration. Notably, oil-emulsion systems display a much lower critical pressure than rigid-particle suspensions because, beyond a threshold capillary pressure $\triangle P_{cap}=2\gamma/r_p$, oil droplets deform and intrude into the pores, generating irreversible fouling [14]. The range $X_3 \in [0.04, 0.06]$ MPa was therefore chosen to keep the system in the sub-critical regime.

Comparative sensitivity: Among the three variables, TMP showed the steepest linear response (Fig. 1c) but also the narrowest safe operating window, whereas stirring rate exhibited the strongest non-linearity, with a clear optimum around 190-250 rpm. The water-to-oil ratio acted as a slowly varying boundary condition that modulates how strongly X_2 and X_3 influence the flux — a coupling that motivates the multivariate BBD analysis in Section 3.2.

3.2 Model fitting and ANOVA

The quadratic polynomial model derived from the 17 experimental runs (Table 2) is expressed as Eq. (3):

Table 2. Box-Behnken design matrix and experimental results

Model	Water-to-oil ratio/(X_1)	Stirring rate/rpm(X_2)	TMP/MPa(X_3)	Permeate flux/L·m^{-2}·h^{-1}
1	8	0	0.05	3.01
2	10	0	0.05	3.04
3	8	380	0.05	3.33
4	10	380	0.05	2.2
5	8	190	0.04	2.46
6	10	190	0.04	2.78
7	8	190	0.06	4.21
8	10	190	0.06	3.43
9	9	0	0.04	2.91
10	9	380	0.04	2.59
11	9	0	0.06	3.89
12	9	380	0.06	3.37
13	9	190	0.05	4.14
14	9	190	0.05	4.21
15	9	190	0.05	4.21
16	9	190	0.05	4.4
17	9	190	0.05	4.24

$$Y=4.24-0.195X_1-0.170X_2+0.520X_3-0.290X_1X_2-0.275X_1X_3 \\ -0.050X_2X_3-0.658X_1^2-0.688X_2^2-0.363X_3^2 \quad (3)$$

ANOVA results (Table 3) confirm the model's validity. The Model F-value of 41.69 and P-value < 0.0001 indicate high significance. The Lack of Fit P-value (0.1030) > 0.05 implies the model adequately fits the data. The coefficient of determination (R^2) is 0.9817, suggesting the model explains 98.17% of the variance. Notably, the interaction term X_1X_2 (water-to-oil ratio and stirring rate) showed a highly significant P-value (<0.01), highlighting the strong coupling between feed composition and hydrodynamics.

3.3 Response surface analysis:interaction of water-to-oil ratio and stirring rate

The interaction between water-to-oil ratio (X_1) and stirring rate (X_2) on permeate flux, with TMP fixed at 0.05 MPa, is illustrated in Fig. 2.

The response surface exhibits a saddle-shaped topology. In the high water-to-oil ratio region (dilute emulsion, Ratio = 10), the surface is relatively flat. Here, the lower oil concentration minimizes cake layer formation [29], rendering the flux less sensitive to shear variations. Although agitation enhances flux, the marginal benefit of shear force diminishes because the primary mass transfer resistance stems from the intrinsic membrane resistance rather than the cake layer. Furthermore, excessive shear rates may induce droplet breakup, reducing droplet size and thereby increasing the risk of pore blocking [30].

Conversely, in the low water-to-oil ratio region (concentrated emulsion, Ratio = 8), the impact of stirring is pronounced. High oil concentrations induce rapid droplet deposition and severe

Table 3. ANOVA results for the permeate flux model

Source	Sum of Squares	df	Mean Square	F-value	P-value	
Model	8.18	9	0.9088	41.69	0.0001	**
A- water-to-oil ratio	0.3042	1	0.3042	13.95	0.0073	**
B-stirring rate	0.2312	1	0.2312	10.61	0.0139	*
C-TMP	2.16	1	2.16	99.23	< 0.0001	**
AB	0.3364	1	0.3364	15.43	0.0057	**
AC	0.3025	1	0.3025	13.88	0.0074	**
BC	0.0100	1	0.0100	0.4587	0.5200	not significant
A^2	1.82	1	1.82	83.50	< 0.0001	**
B^2	1.99	1	1.99	91.29	< 0.0001	**
C^2	0.5533	1	0.5533	25.38	0.0015	*
Residual	0.1526	7	0.0218			
Lack of Fit	0.1152	3	0.0384	4.11	0.1030	not significant
Pure Error	0.0374	4	0.0094			
Cor Total	8.33	16				

Note: **, P< 0.01 highly significant; *, P< 0.05 significant
Model: **P < 0.0001**(Significant)
X_1X_2 Interaction: **P = 0.0057** (Significant)
R^2: 0.9817
Adj **R^2**: 0.9581

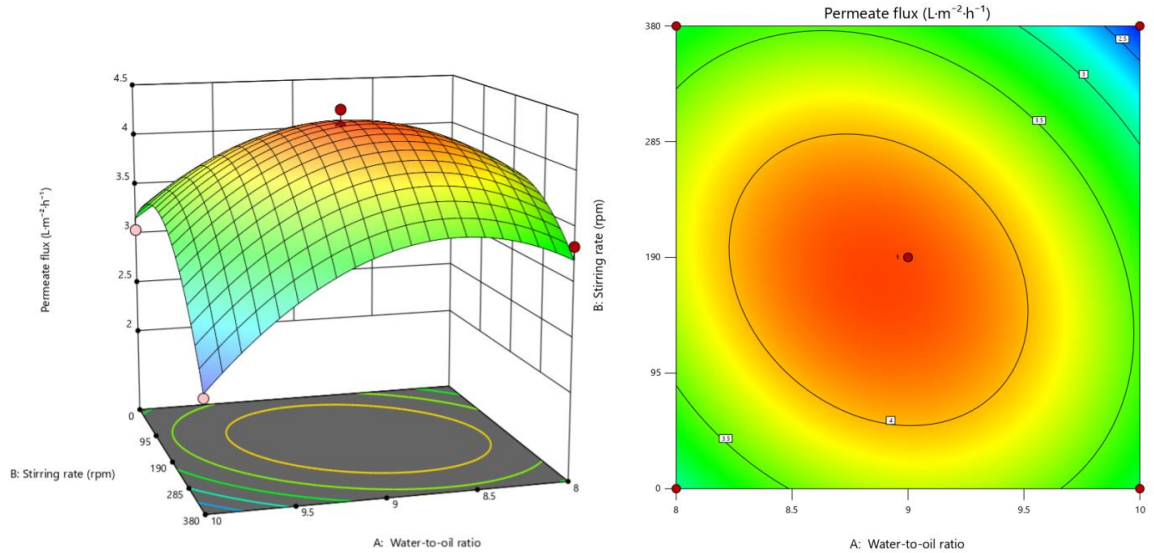

Figure 2. Effect of water-to-oil ratio (X_1) and stirring rate (X_2) on permeate flux: 3D response surface and 2D contour maps

concentration polarization [31]. Under these conditions, the shear force generated by higher stirring rates is critical for scouring surface deposits and reducing mass transfer resistance. This

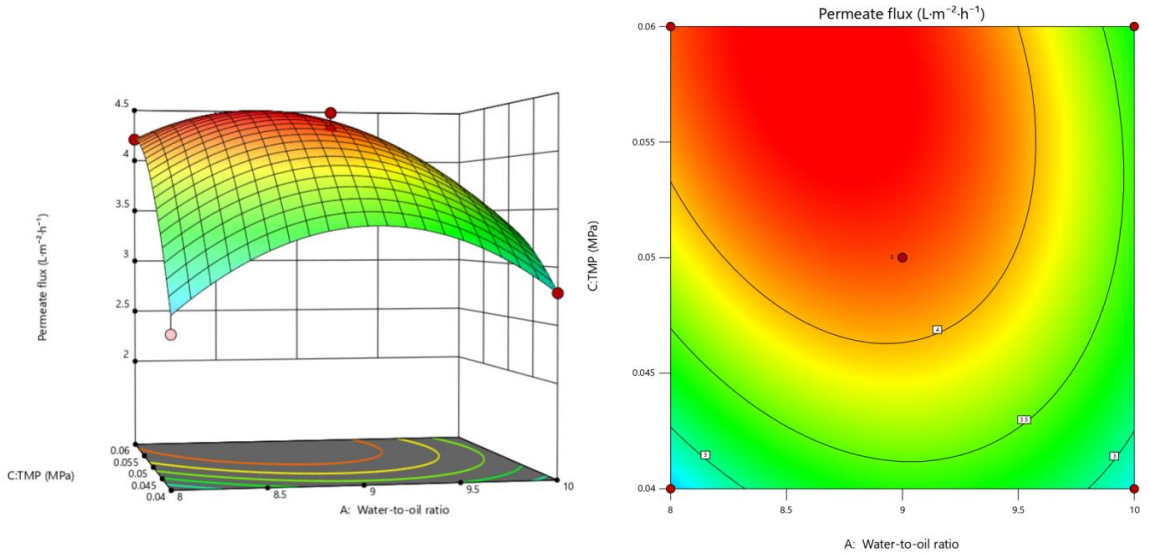

Figure 3. Effect of water-to-oil ratio (X_1) and transmembrane pressure (X_3) on permeate flux: 3D response surface and 2D contour maps

significant interaction reveals that hydrodynamic optimization is most critical when treating concentrated emulsions.

The saddle-shaped response surface can be rationalized by considering the competition between two characteristic time scales: the convective deposition time $\tau_{dep}=\frac{\delta}{\upsilon_w}$ (where $\upsilon_w=\frac{J}{A}$ is the permeation velocity and δ the cake thickness) and the shear-induced removal time $\tau_{rem}\sim\mu/\tau_w$ (with τ_w the wall shear stress). At high X_1 (dilute feed), τ_{dep} is intrinsically long because the volumetric oil load is low; the system therefore operates near the "shear-saturated" regime, where additional shear yields diminishing returns. Conversely, at low X_1 (concentrated feed), τ_{dep} shortens dramatically, and the ratio τ_{rem}/τ_{dep} becomes the rate-limiting parameter. This explains why the X_1-X_2 interaction term is highly significant ($P = 0.0057$): the shear requirement scales with the feed concentration. Compared with the surfactant-stabilized emulsion system reported by Deng et al. [24], where electrostatic droplet-membrane interactions dominate, our surfactant-free metastable emulsion is governed almost exclusively by hydrodynamic-mechanical coupling — a distinction that explains the higher FRR (94.88%) achieved here.

3.4 Response surface analysis: interaction of water-to-oil ratio and transmembrane pressure

In the dilute solution regime, flux increases linearly with TMP, consistent with pressure-controlled filtration. However, in the concentrated emulsion regime, flux enhancement diminishes rapidly with increasing pressure. This phenomenon arises from the dual effects of high concentration and pressure, which compact the cake layer and reduce porosity. Critically, excessive TMP may overcome the interfacial tension of oil droplets [32], inducing droplet deformation and forcing them into membrane pores. This leads to irreversible fouling [33]. Therefore, moderate operating

pressures are superior for concentrated emulsions to prevent pore blocking [34].

Mechanistic synthesis. The pressure-induced flux saturation observed at low X_1 can be quantitatively described by the droplet intrusion criterion: an oil droplet of radius r_d deforms and enters a pore of radius r_p when the applied TMP exceeds the critical capillary pressure:

$$\triangle P_{cap}=\frac{2\gamma|\cos\theta_{ow}|}{r_p}(1-\frac{r_p}{r_d}) \tag{4}$$

where γ is the oil-water interfacial tension and θ the contact angle on the hydrophilic PTFE surface. Substituting $\gamma \approx 30$mN/m, $r_p = 0.11$μm, $r_d \approx 3.75$μm, and underwater oil contact angle $\theta_{ow} \approx 150°$ (consistent with the hydrophilic PTFE surface, which is oleophobic underwater), yields $\triangle P_{cap} \approx 0.46$MPa, well above our operating window. However, in the concentrated regime the local TMP at the cake-membrane interface is amplified by cake compaction, effectively lowering the macroscopic pressure threshold. This rationalizes why pore intrusion is observed below 0.06 MPa only at low X_1 — a phenomenon consistent with recent CFD-population-balance simulations [26].

Numerical optimization was conducted to maximize permeate flux while keeping variables within range. The optimal conditions were identified as: Water-to-Oil Ratio (X_1) 8.5, stirring rate (X_2) 213 rpm, Transmembrane Pressure (X_3) 0.059 MPa.

The model predicted a maximum flux of 4.46 $L \cdot m^{-2} \cdot h^{-1}$. Validation experiments (**n=3**) yielded an average flux of 4.37 $L \cdot m^{-2} \cdot h^{-1}$, reflecting a relative error of 2.06%. This confirms the model's accuracy and predictive reliability.

3.5 Performance verification: comparison with gravity settling

In order to comprehensively evaluate the actual efficiency of the optimal process conditions obtained through RSM optimization, we conducted a parallel comparison experiment with the traditional gravity method under the optimal parameter combination (X_1=8.5, X_2=213 rpm, X_3= 0.059MPa) and evaluated the short-term operational stability of the membrane.

We prepared a batch of emulsion formed under the optimal stirring intensity. It was divided into two portions: one for the membrane separation system, and the other poured into a 500 mL separatory funnel for static gravity stratification. The membrane separation system began to continuously produce highly clarified permeate immediately upon operation, and the treatment of the entire batch was completed in 1 minute and 18 seconds. In contrast, for the sample used for gravity stratification, even after a standing time of >24 hours, in addition to the oil droplets adhering to the cup wall, magnification still reveals fine oil phase droplets remained in the lower water layer (as shown in Fig. 4).

More importantly, there is a difference in product purity (see Table 4). Under optimal conditions, the oil content in the membrane separation permeate was as low as <50 ppm, far superior to the oil content of up to 300 ppm still present in the so-called "clarified" aqueous phase after gravity stratification. We sampled and analyzed the emulsified layer produced by the gravity method and found that it consisted of a large number of fine oil droplets with an average particle size in the range of 5-10 μm, which is the root cause of the low efficiency of traditional methods.

This comparison vividly demonstrates that the optimized membrane separation process not only achieves an order-of-magnitude improvement in separation speed but also fundamentally solves the problem of the interfacial emulsion layer, greatly improving product purity and material recovery rates.

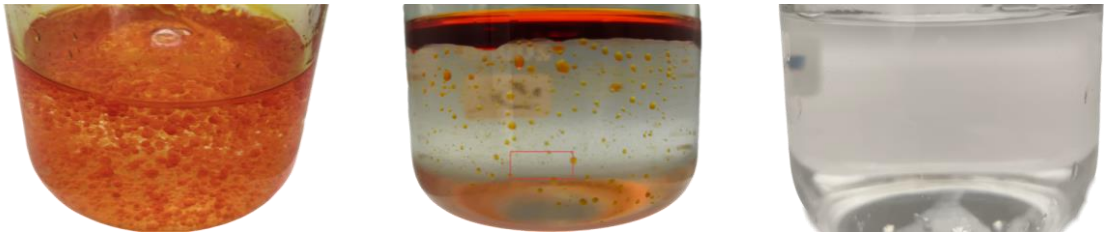

(a) Initial emulsion state immediately after mixing

(b) Separation status after standing for > 24 h

c)The filtrate produced immediately by the membrane separation system

Figure 4. Comparison of gravity stratification. (a) Initial emulsion state immediately after mixing; (b) Separation status after standing for > 24 h, showing a distinct interface, revealing residual fine oil droplets; (c) The filtrate produced immediately by the membrane separation system, the filtrate is clear and transparent

Table 4. Performance comparison under optimal conditions

Performance index	Membrane separation (optimized)	Gravity stratification (24 hours)
Separation time	Instant	>24 hours
Emulsion layer	None	Approx. 6% volume
Aqueous phase oil content	< 50 ppm	Approx. 300 ppm
Recovery rate	> 99%	< 90%

To further evaluate the membrane's anti-fouling performance under the optimal operating conditions, the Flux Recovery Ratio (FRR) was analyzed. After the separation experiment, the fouled membrane was physically rinsed with deionized water to remove the loose cake layer, Subsequently, immerse the membrane in anhydrous ethanol for ten minutes to dissolve any residual organic contaminants. The pure water flux of the cleaned membrane (J_r) was then measured under the same pressure conditions as the initial pure water flux (J_0). The FRR was calculated using Eq. (5):

$$\mathrm{FRR} = \frac{J_r}{J_0} \times 100\% \tag{5}$$

Meanwhile, to further clarify how the stirring rate (X_2) reduces the resistance of the filter cake layer, the resistance model was analyzed using Darcy's law [35]. This resistance model was derived from Eqs. (6-10) [36]:

Total resistance (R_t):

$$R_t = R_m + R_c + R_{ir} \tag{6}$$

Intrinsic membrane resistance (R_m):

$$R_m = \frac{\triangle P}{\mu_w \cdot J_0} \tag{7}$$

Total resistance (R_t):

$$R_t = \frac{\triangle P}{\mu_e \cdot J} \tag{8}$$

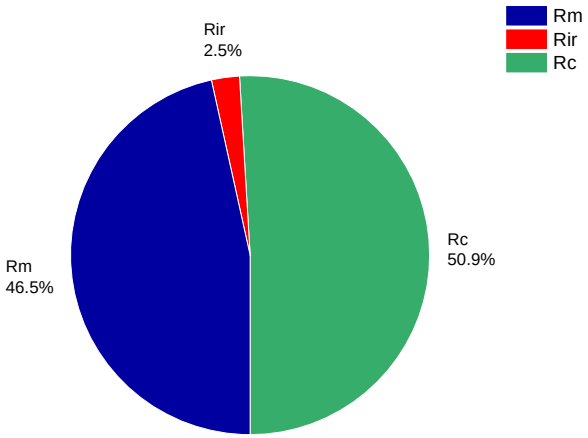

Figure 5. Distribution of filtration resistance components based on the resistance-in-series model under the optimal operating conditions (X_1=8.5, X_2=213rpm, X_3=0.059MPa)

Irreversible fouling resistance (R_{ir}):

$$R_{ir} = \frac{\triangle P}{\mu_w \cdot J_r} - R_m \tag{9}$$

Cake resistance (R_c):

$$R_c = R_t - R_m - R_{ir} \tag{10}$$

Calculated: Total resistance (R_t): 5.46×10^{13}m^{-1} (100%)
Intrinsic membrane resistance(R_m): 2.54×10^{13}m^{-1} (46.51%)
Cake resistance (R_c): 2.78×10^{13}m^{-1} (50.97%)
Irreversible fouling resistance (R_{ir}): 1.37×10^{12}m^{-1} (2.51%)

The experimental results showed an FRR of 94.88%. This high recovery rate indicates that the fouling formed under the optimized conditions (Ratio=8.5, TMP=0.059 MPa) was predominantly reversible. Analysis based on the resistance-in-series model [37, 38], derived from the Darcy-Poiseuille law, demonstrates that the optimal stirring shear rate of 213 rpm not only maintains a high steady-state flux but also significantly minimizes the probability of oil droplets penetrating the membrane pores. Quantitative calculations reveal that the irreversible fouling resistance (R_{ir}), which represents internal pore blocking, accounts for merely 2.51% of the total resistance. Instead, the fouling resistance is predominantly governed by the reversible cake layer resistance (R_c, accounting for approximately 50.97%) deposited on the membrane surface (as shown in Fig. 5) [39]. This distribution explains why a remarkable flux recovery ratio (FRR) of 94.88% was successfully achieved through simple physical rinsing combined with short-term chemical cleaning. Ultimately, the quantitative evaluation of the resistance model provides compelling mechanistic evidence for the efficacy of the optimized hydrodynamic parameters in mitigating membrane fouling. The effective combination of hydrophilic PTFE membrane material and optimized hydrodynamic shear force successfully minimized irreversible fouling such as pore plugging [40]. The membrane maintained excellent hydraulic performance after cleaning, demonstrating its potential for long-term industrial cycles.

Comparison with literature. The FRR of 94.88% achieved here is comparable to or superior to recent values reported for surface-modified PES (87-92%, Safarpour et al. [28]) and ceramic based O/W systems (90-94%, Wu et al. [41]), despite our use of an unmodified commercial PTFE membrane. This benchmarking suggests that hydrodynamic optimization can deliver anti-fouling performance equivalent to material-level engineering, but at a fraction of the cost — a finding with direct industrial relevance.

4. Discussion

Industrial implications. The optimized hydrodynamic envelope ($X_1 \approx 8.5$, $X_2 \approx 213$ rpm, $X_3 \approx 0.059$ MPa) translates directly into design guidance for stirred or rotating-disk membrane modules used in fine-chemical washing trains. For the thionocarbamate process, replacing the existing gravity-settling stage with a stirred-cell membrane unit is projected to reduce the unit operation footprint and shorten the residence time by more than two orders of magnitude (from >8 h to ~1 min), while improving aqueous-phase product recovery from <90% to >99% (Table 4).

Scalability considerations. The dimensionless wall shear rate $\dot{\gamma}_w$ is the key scale-up criterion. Maintaining the optimal $\dot{\gamma}_w$ of approximately 1500 s^{-1} in larger modules requires either rotating-disk or vibratory shear-enhanced (VSEP) configurations [38], because impeller-only stirring becomes inefficient beyond a few liters. Energy consumption scales roughly with $\dot{\gamma}_w^2$, so trade-offs between flux and specific energy demand (kWh·m^{-3} permeate) must be re-optimized at pilot scale.

Limitations of the present study:

(1) The model is calibrated for one specific oil chemistry (thionocarbamate) and one membrane (0.22 μm PTFE); transferring it to other oils requires re-evaluation of γ, θ, and droplet rheology.

(2) The 1-min averaging window captures the initial flux but not long-term fouling dynamics; long-duration tests (>24 h) under cyclic cleaning are needed before industrial deployment.

(3) RSM is a local approximation around the design center; extrapolation beyond the BBD bounds is not advised.

Knowledge gaps and future directions. Three avenues stand out:

(a) Coupling RSM with mechanistic population-balance models to predict droplet size evolution under shear.

(b) Extending the framework to surfactant-laden industrial feeds, where DLVO-type droplet-membrane interactions become non-negligible [42].

(c) Integrating real-time fouling sensors and machine learning based control [43] to enable closed loop hydrodynamic adjustment in continuous operation. Addressing these gaps will move stirred cell membrane separation from a laboratory optimization exercise toward a digitally controlled, industrially robust unit operation.

5. Conclusions

A second-order response surface model was successfully established to describe the stirred-cell membrane separation of O/W emulsions. The model demonstrated a high goodness of fit ($R^2 > 0.98$), facilitating accurate performance prediction.

Significant interaction mechanisms were elucidated: for high-concentration emulsions, increasing the stirring rate is essential to mitigate concentration polarization. Simultaneously, transmembrane

pressure must be carefully controlled to prevent cake layer compaction and droplet deformation-induced pore penetration.

Global optimal parameters were determined as a water-to-oil ratio of 8.5, stirring rate of 213 rpm, and TMP of 0.059 MPa. Under these conditions, the permeate flux reached 4.37 $L \cdot m^{-2} \cdot h^{-1}$. The optimized process effectively eliminates the interfacial emulsified layer issues associated with gravity settling, demonstrating substantial industrial potential.

Acknowledgments

This research was supported by the Principal Fund Project of Qingdao West Coast New Area (No. 39100301).

References

1. Gupta, R.K., Dunderdale, G.J., England, M.W., Hozumi, A. (2017). Oil/water separation techniques: a review of recent progresses and future directions. Journal of Materials Chemistry A, 5(31), 16025-16058. https://doi.org/10.1039/c7ta02070h
2. Kaya, D., Hung, Y.T. (2021). Advances in treatment of vegetable oil refining wastes. Environmental and Natural Resources Engineering, 325-375. https://doi.org/10.1007/978-3-030-54626-7_8
3. Bulatovic, S.M. (2010). Handbook of Flotation Reagents: Chemistry, Theory and Practice. Elsevier. https://doi.org/10.1016/c2009-0-17331-2
4. Burdonov, A., Vchislo, N., Verochkina, E., Rozentsveig, I. (2023). Synthesis of new dithiocarbamate and xanthate complexes and their application in enrichment processes. Izvestiya Vuzov. Prikladnaya Khimiya i Biotekhnologiya, 13(2), 160-171. https://doi.org/10.21285/2227-2925-2023-13-2-160-171
5. Tian, Y., Zhou, J., He, C., He, L., Li, X., Sui, H. (2022). The formation, stabilization and separation of oil-water emulsions: a review. Processes, 10(4), 738. https://doi.org/10.3390/pr10040738
6. Chen, Y., Narayan, S., Dutcher, C.S. (2020). Phase-dependent surfactant transport on the microscale: Interfacial tension and droplet coalescence. Langmuir, 36(49), 14904-14923. https://doi.org/10.1021/acs.langmuir.0c02476
7. Goodarzi, F., Zendehboudi, S. (2019). A comprehensive review on emulsions and emulsion stability in chemical and energy industries. The Canadian Journal of Chemical Engineering, 97(1), 281-309. https://doi.org/10.1002/cjce.23336
8. Gong, J., Xiang, B., Sun, Y., Li, J. (2023). Janus smart materials with asymmetrical wettability for on-demand oil/water separation: A comprehensive review. Journal of Materials Chemistry A, 11(46), 25093-25114. https://doi.org/10.1039/d3ta04160c
9. Baig, N., Sajid, M., Salhi, B., Abdulazeez, I. (2023). Special wettable membranes for oil/water separations: a brief overview of properties, types, and recent progress. Colloids and Interfaces, 7(1), 11. https://doi.org/10.3390/colloids7010011
10. Lee, U., Kandel, D.R., Kwak, D., Tran, H.M., Lee, J. (2025). Superhydrophilic and antifouling PDA/TA-MOF nanocomposite PTFE membranes for efficient and sustainable treatment of dissolved oil-containing wastewater. Desalination, 593, 119688. https://doi.org/10.1016/j.desal.2025.119688
11. Xiang, B., Sun, Q., Zhong, Q., Mu, P., Li, J. (2022). Current research situation and future prospect of superwetting smart oil/water separation materials. Journal of Materials Chemistry A, 10(38), 20190-20217. https://doi.org/10.1039/d2ta04469b
12. Cui, Z., Jiang, Y., Field, R.W. (2010). Fundamentals of pressure-driven membrane separation processes. In Membrane Technology (pp. 1-18). Elsevier. https://doi.org/10.1016/b978-1-85617-632-3.00001-x
13. Schuch, A., Deiters, P., Henne, J., Köhler, K., Schuchmann, H.P. (2013). Production of W/O/W

(water-in-oil-in-water) multiple emulsions: droplet breakup and release of water. Journal of Colloid and Interface Science, 402, 157-164. https://doi.org/10.1016/j.jcis.2013.03.066
14. Galvagno, M., Ramon, G.Z. (2020). Hydrodynamic-colloidal interactions of an oil droplet and a membrane surface. Langmuir, 36(11), 2858-2864. https://doi.org/10.1021/acs.langmuir.9b03778
15. Yala, S.A., Pillay, V.L. (2025). The effect of fluid dynamics and fluid–particle interactions on the characteristics of fouling layers in membrane filtration systems-a review. Journal of Membrane Science and Research, 11(1), e717535. https://doi.org/10.22079/jmsr.2024.2029587.1663
16. Szpisják-Gulyás, N., Al-Tayawi, A.N., Horváth, Z.H., László, Z., Kertész, S., Hodúr, C. (2023). Methods for experimental design, central composite design and the Box-Behnken design, to optimise operational parameters: A review. Acta Alimentaria, 52(4), 521-537. https://doi.org/10.1556/066.2023.00235
17. Shahabadi, S.M.S., Reyhani, A. (2014). Optimization of operating conditions in ultrafiltration process for produced water treatment via the full factorial design methodology. Separation and Purification Technology, 132, 50-61. https://doi.org/10.1016/j.seppur.2014.04.051
18. Waqas, S., Harun, N.Y., Arshad, U., Laziz, A.M., Mun, S.L.S., Bilad, M.R., Nordin, N.A.H., Alsaadi, A.S. (2024). Optimization of operational parameters using RSM, ANN, and SVM in membrane integrated with rotating biological contactor. Chemosphere, 349, 140830. https://doi.org/10.1016/j.chemosphere.2023.140830
19. Susan, K., Ali, A. (2018). Using response surface methodology and Box-Behnken design in the study of affecting factors on the dairy wastewater treatment by MEUF. Membrane and Water Treatment, 9(5), 335-342. https://doi.org/10.12989/mwt.2018.9.5.335
20. Li, L., Zhang, S., He, Q., Hu, X. (2015). Application of response surface methodology in experiment design and optimization. Research and Exploration in Laboratory, 34(8), 41-45. https://doi.org/10.3969/j.issn.1006-7167.2015.08.011
21. Ward, L.M., Martin, C.C., Weinman, S.T. (2025). Pattern size relative to oil droplet size effect on oil fouling in nanofiltration. Journal of Membrane Science, 715, 123457. https://doi.org/10.1016/j.memsci.2024.123457
22. Alsaady, M. (2025). Optimization of operating parameters using response surface methodology for CO2/CH4 separation using polysulfone/NH2-MIL-125 (Ti) mixed matrix membrane. ACS Omega, 10(39), 45050-45061. https://doi.org/10.1021/acsomega.5c03815
23. Li, Y., Li, Y., Liu, D., Wang, Y., Chen, J., Ma, Y., Gao, Y., Ding, D., Xiao, G. (2023). Preparing ceramic membranes for oil-in-water emulsions separation with oil-based drilling cutting pyrolysis residues (ODPRs) as raw material. Ceramics International, 49(19), 31559-31568. https://doi.org/10.1016/j.ceramint.2023.07.107
24. Deng, Y., Dai, M., Wu, Y., Peng, C. (2023). Emulsion system, demulsification and membrane technology in oil-water emulsion separation: A comprehensive review. Critical Reviews in Environmental Science and Technology, 53(12), 1254-1278. https://doi.org/10.1080/10643389.2022.2131340
25. Wollborn, T., Luhede, L., Fritsching, U. (2019). Evaluating interfacial shear and strain stress during droplet deformation in micro-pores. Physics of Fluids, 31(1), 012109. https://doi.org/10.1063/1.5064858
26. Xu, Z., Wang, T., Che, Z. (2020). Droplet deformation and breakup in shear flow of air. Physics of Fluids, 32(5), 052109. https://doi.org/10.1063/5.0006236
27. Zhong, C., Wang, Z. (2024). A three-mechanism (intermediate pore blocking, standard pore blocking and cake filtration) model considering correction of effective filtration area. Journal of Environmental Chemical Engineering, 12(5), 113654. https://doi.org/10.1016/j.jece.2024.113654
28. Safarpour, M., Hosseinpour, S., Haddad Irani-nezhad, M., Orooji, Y., Khataee, A. (2022). Fabrication of Ti2SnC-MAX phase blended PES membranes with improved hydrophilicity and antifouling properties for oil/water separation. Molecules, 27(24), 8914. https://doi.org/10.3390/molecules27248914
29. Ghaffour, N., Qamar, A. (2020). Membrane fouling quantification by specific cake resistance and flux enhancement using helical cleaners. Separation and Purification Technology, 239, 116587. https://doi.

org/10.1016/j.seppur.2020.116587
30. Teow, Y.H., Wong, Z.H., Takriff, M.S., Mohammad, A.W. (2018). Fouling behaviours of two stages microalgae/membrane filtration system applied to palm oil mill effluent treatment. Membrane and Water Treatment, 9(5), 373-383. https://doi.org/10.12989/mwt.2018.9.5.373
31. Chen, J. C., Li, Q., Elimelech, M. (2004). In situ monitoring techniques for concentration polarization and fouling phenomena in membrane filtration. Advances in Colloid and Interface Science, 107(2-3), 83-108. https://doi.org/10.1016/j.cis.2003.10.018
32. Needham, D., Kinoshita, K., Utoft, A. (2019). Micro-surface and-interfacial tensions measured using the micropipette technique: applications in ultrasound-microbubbles, oil-recovery, lung-surfactants, nanoprecipitation, and microfluidics. Micromachines, 10(2), 105. https://doi.org/10.3390/mi10020105
33. Chu, K.H., Yoo, S.S., Yoon, Y., Ko, K.B. (2015). Specific investigation of irreversible membrane fouling in excess of critical flux for irreversibility: A pilot-scale operation for water treatment. Separation and Purification Technology, 151, 147-154. https://doi.org/10.1016/j.seppur.2015.07.033
34. Racz, G., Kerker, S., Schmitz, O., Schnabel, B., Kovacs, Z., Vatai, G., Ebrahimi, M., Czermak, P. (2015). Experimental determination of liquid entry pressure (LEP) in vacuum membrane distillation for oily wastewaters. Membrane and Water Treatment, 6(3), 237-249. https://doi.org/10.12989/mwt.2015.6.3.237
35. Huisman, I.H., Dutrê, B., Persson, K.M., Trägårdh, G. (1997). Water permeability in ultrafiltration and microfiltration: Viscous and electroviscous effects. Desalination, 113(1), 95-103. https://doi.org/10.1016/s0011-9164(97)00118-5
36. Moshafi, S., Fong, D., Jiang, Y., Sanaei, P. (2026). Effects of cake formation on flow and transport in a pleated membrane filter. Journal of Engineering Mathematics, 156(1), 13. https://doi.org/10.1007/s10665-025-10500-4
37. Frederic, E., Guigui, C., Jacob, M., Machinal, C., Krifi, A., Line, A., Schmitz, P., Machinal, A.K. (2018). Modelling of fluid flow distribution in multichannel ceramic membrane: Application to the filtration of produced water. Journal of Membrane Science, 567, 280-289. https://doi.org/10.1016/j.memsci.2018.09.021
38. Du, X., Wang, Y., Leslie, G., Li, G., Liang, H. (2017). Shear stress in a pressure-driven membrane system and its impact on membrane fouling from a hydrodynamic condition perspective: a review. Journal of Chemical Technology & Biotechnology, 92(3), 463-478. https://doi.org/10.1002/jctb.5154
39. Gao, S., Zhong, C., Wang, Z. (2022). A model describing the pressure drops across the membrane and cake layers for constant flux cross-flow microfiltration process. Journal of Environmental Chemical Engineering, 10(3), 107984. https://doi.org/10.1016/j.jece.2022.107984
40. Alseksek, Y.K., Arumugham, T., Hasan, S.W. (2025). Ultrafiltration membrane based on PES/CeO2-MoS2 heterostructured nanocomposites for enhanced oil-in-water emulsion separation and antifouling. Separation and Purification Technology, 367, 132921. https://doi.org/10.1016/j.seppur.2025.132921
41. Wu, X., Fang, M., Li, G. (2025). Fouling mitigation of silicon carbide membranes by pre-deposited dynamic membranes for the separation of oil-in-water emulsions. Membranes, 15(7), 195. https://doi.org/10.3390/membranes15070195
42. Nagasawa, H., Omura, T., Asai, T., Kanezashi, M., Tsuru, T. (2020). Filtration of surfactant-stabilized oil-in-water emulsions with porous ceramic membranes: Effects of membrane pore size and surface charge on fouling behavior. Journal of Membrane Science, 610, 118210. https://doi.org/10.1016/j.memsci.2020.118210
43. Nazari, S., Abdelrasoul, A. (2025). Advancements and applications of artificial intelligence and machine learning in material science and membrane technology: A comprehensive review. Membranes, 15(12), 353. https://doi.org/10.3390/membranes15120353